Submitted to Advanced Engineering Materials, April 2022

On the Friction Stir Processing of Additive Manufactured 316L Stainless Steel

Seyed Vahid Sajadifar[a], *Ali Hosseinzadeh*[b], *Julia Richter*[a], *Marcel Krochmal*[a], *Thomas Wegener*[a], *Artjom Bolender*[a], *Akbar Heidarzadeh*[c], *Thomas Niendorf*[a], *Guney Guven Yapici*[b,*]

[a] University of Kassel, Institute of Materials Engineering, Mönchebergstraße 3, 34125 Kassel, Germany

[b] Mechanical Engineering Department, Ozyegin University, Istanbul, 34794, Turkey

[c] Department of Materials Engineering, Azarbaijan Shahid Madani University, Tabriz 53714-161, Iran

*Corresponding Author Tel.: +90 216 564 9115; Fax: +90 216 564 9057

E-mail address: guven.yapici@ozyegin.edu.tr

Abstract: The novel combination of friction stir processing (FSP) and additive manufacturing (AM) was studied in present work. Laser-based powder bed fusion of metals (PBF-LB/M) was employed to establish 316L stainless steel with a bimodal microstructure. Upon FSP, the as-built bimodal microstructure with an average grain size of 179 µm was transformed into a unimodal microstructure containing ultra-fine grains with an average grain size of 1.2 µm. Results obtained by mechanical testing revealed that after FSP; the hardness, the yield point and the ultimate strength of additively manufactured 316L were enhanced by 45%, 77% and 62%, respectively. Microstructure assessment revealed that such a unique improvement in the mechanical properties was due to considerable structural refinement leading to grain boundary strengthening. Energy-dispersive X-ray diffraction analysis revealed that phase transformation did not occur upon FSP. Fracture analysis further indicated that severe plastic deformation (SPD) during FSP can promote the transformation of coarse voids to fine voids and, hence, densification of as-built parts.

Keywords: Laser powder bed fusion; Friction stir processing; Microstructure; Strength; Mechanical properties; Fracture

1. Introduction

Excellent corrosion resistance and superior mechanical properties of 316L stainless steel qualify this alloy for various applications from biomedical to petrochemical industries [1]–[4]. Due to the addition of molybdenum, the corrosion performance of 316L stainless steel was found to be even better than that of the 304L alloy [5]–[7]. 316L stainless steel is also characterized by high strain hardening, pointing at good workability, as well as acceptable weldability broadening the number of potential engineering applications [8]–[11]. However, the material (especially in the as-cast condition)

suffers from a poor yield strength (YS) like numerous austenitic alloys [12]. A promising technology to overcome this strength-ductility trade-off is additive manufacturing (AM). Among different AM methods, laser-based powder bed fusion of metals (PBF-LB/M) combines the fabrication of near-net shape components of complex geometry with excellent mechanical properties [4][13]–[16]. The PBF-LB/M process is based on the consecutive consolidation of metallic powders by a laser and the repetitive fusing of thin layers on top of each other [17]–[19].

For years, the processability and the corresponding mechanical properties of 316L stainless steel parts fabricated via PBF-LB/M have been in the focus of investigations [4][20]–[22]. Most of these research works tried to optimize AM parameters (e.g., laser power, hatch spacing and building direction) in order to directly design superior microstructures and, hence, mechanical properties. Generally, the influence of laser power on the mechanical properties and microstructure of 316L stainless steel was more noticeable than other processing parameters such as building direction and hatch spacing due to its dominant influence on the thermal history [21]. By the utilization of different laser powers, mechanical properties and microstructure of this alloy were successfully tailored [4][13]. In any case the processed material exhibits relatively coarse, columnar grains after PBF-LB/M. Nevertheless, in comparison to conventionally manufactured counterparts the PBF-LB/M specimens reveal an increased strength with retained high ductility. The high strength is mainly attributed to the intrinsic cooling conditions. Small melt pool sizes combined with consecutive melting of individual layers in this manufacturing process result in high cooling rates up to 10^6 K/s eventually promoting high internal stresses. Those stresses induced by the intrinsic heat treatment and thermal history promote the evolution of a dislocation network and subgrain structures, respectively, wherefore the YS is increased. It was already reported that such subgrains play a key role in grain boundary engineering (GBE) of additively manufactured components [23][24].

A combination of various AM parameters (i.e., different scanning speeds ranging from 400 mm/s to 800 mm/s and laser power ranging from 40 W to 70 W) and post-process thermomechanical treatments i.e., strain- annealing cycles, were already utilized for GBE of 316L [22]. It was observed that the stored energy in a 7.7 % deformed microstructure was adequate to drive the onset of recrystallization in this alloy. Besides, attaining control over the solute segregation at cell boundaries in PBF-LB/M processing was found to be crucial to completely recrystallize the microstructure and increase the twin boundary fraction. Higher scanning speed shortened the available time for diffusion and eventually promoted the solute segregation at cell boundaries retarding the occurrence of recrystallization and hindering the formation of deformation twins. Since cell boundaries containing solutes acted as dislocation sinks, the critical stress required for deformation twinning rose. However, lower scanning speed caused a coarser cellular structure eventually promoting nucleation and growth of newly recrystallized grains.

Previously, friction stir processing (FSP) as a severe plastic deformation (SPD) technique was used to improve the strength of 316L stainless steel fabricated by conventional methods [2][25]–[27]. Despite 50% reduction in elongation at failure (EF), FSP could increase YS and ultimate tensile strength (UTS) of the base metal 316L alloy 1.6 and 1.2 times, respectively [26]. Another study showed that optimization of process parameters in FSP of 316L stainless steel can even result in nanograins with sizes below 200 nm [2]. Due to the noticeable refinement level, twofold rise in wear resistance and threefold rise in hardness were achieved. The increase in the strength and hardness of this alloy upon FSP was rationalized by the well-known grain boundary (GB) strengthening mechanism.

Recently, the feasibility of enhancing the mechanical properties of additively manufactured metals in general and 316L stainless steel in particular via various SPD methods such as FSP, friction stir welding (FSW), equal channel angular extrusion/pressing (ECAE/P) and high-pressure torsion (HPT) has attracted attention [28]–[34]. During SPD, fragmentation and recrystallization of additively manufactured microstructures led to the formation of ultra-fine grained (UFG) materials showing outstanding mechanical behavior. A very recent study showed that FSP has a great potential towards enhancing mechanical properties of additively manufactured 316L stainless steel since this process could improve tensile strength by 18 % with only minimum loss in ductility [33].

In the present work, FSP as a surface modification technique was applied to as-built 316L stainless steel to form a unique microstructure containing ultra-fine and equiaxed grains. Based on the promising findings obtained herein, the UFG microstructure introduced via FSP results in superior mechanical behavior benefiting the envisaged applications for additively manufactured 316L stainless steel. Mechanical behavior and microstructural evolution elaborated in the present study were exploited to establish process-microstructure-property relationships. These relationships will assist to pave the path for densification and improvement of the mechanical properties in additively manufactured components via processing by SPD techniques.

2. Experimental Procedure

2.1. Laser-Based Powder Bed Fusion

Plates of 316L stainless steel were fabricated via PBF-LB/M utilizing a SLM280^{HL} machine by SLM Solutions GmbH (Lübeck, Germany). The SLM280^{HL} machine is equipped with both 400 W and 1000 W lasers and provides a build chamber size of 280 × 280 × 365 mm^3. 316L powder supplied by TLS Technik (Bitterfeld, Germany) with the particle size distribution of 20 – 63 μm was processed in the chamber filled with argon gas. During PBF-LB/M, a laser power of 325 W, a layer thickness of 50 μm, a hatch spacing of 120 μm and a scanning speed of 800 mm/s were chosen. The base plate was heated up to 200 °C. The scanning strategy comprised a rotation of 90°

in each consecutive layer. Plates of 316L with the dimensions of 40 × 3 × 100 mm^3 were manufactured via PBF-LB/M (the 100 mm axis being alongside build direction (BD)).

2.2. Friction Stir Processing

The base material (BM) used for FSP was the 316L stainless steel plate fabricated via PBF-LB/M. To conduct FSP, a conventional milling machine was employed. A tool made of WC-5%CO composed of a shoulder with a diameter of 15 mm, a pin with a diameter of 3 mm and a height of 1.7 mm was utilized for single-pass FSP. Traverse and rotational speeds were kept constant at 85 mm/min, and 1180 rpm, respectively. The tilt angle (the angle between tool axis and normal direction of the plate surface) was set to 2°.

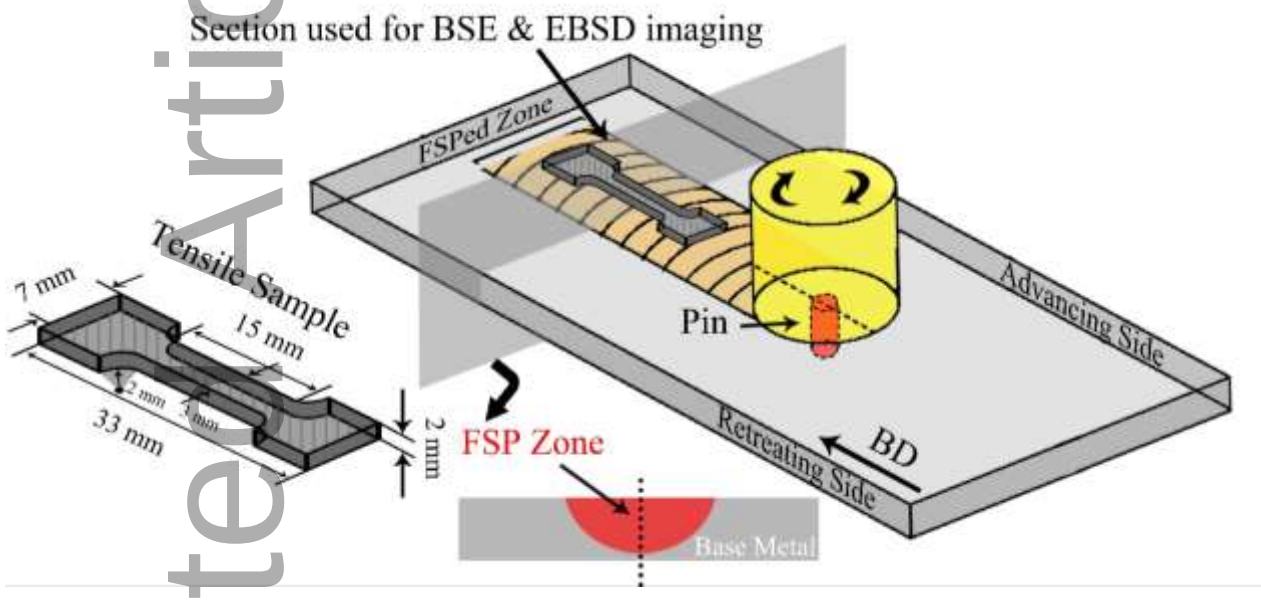

Figure 1. Schematic of the FSP setup used including the geometry of the tensile sample highlighting most relevant characteristics of the process. The plate being treated was initially manufactured by PBF-LB/M, the build direction (BD) is marked by an arrow. The dimensions of the specimens used for tensile testing are shown to the left of the image.

2.3. Mechanical Testing

Microhardness and tensile tests were employed for characterization of the mechanical properties of as-built and FSP conditions. The reported microhardness values for each condition are the average of five indents taken from five different locations of the specimen. Vickers microhardness tests were performed by applying 500 gram-force (gf) on the specimen surface for a duration of 15 s. Flat dog-bone shaped specimens with a gauge length of 15 mm and loading axis parallel to the processing direction (PD) and build direction (BD), respectively, (cf. **Figure 1**) were electro-discharge machined (EDM). For removing residual layers affected by EDM, specimens were ground to 2500 grit using SiC abrasive papers. Tensile experiments were conducted at room

temperature under a nominal strain rate of 0.001 s^{-1}. An extensometer with a gauge length of 12.5 mm was used to measure strain values.

2.4. Microstructure Analysis

Microstructural evolution was analyzed using an optical microscope (OM) and a Zeiss ULTRA GEMINI scanning electron microscope (SEM) operating at a nominal voltage of 20 kV equipped with an electron backscatter diffraction (EBSD) unit. Beraha's BII reagent was utilized to etch the specimens. A CamScan MV 2300 SEM operating at a nominal voltage of 20 kV was employed in both back-scattered electron (BSE) and secondary electron (SE) modes for capturing microstructural evolution and fracture surfaces, respectively. Specimens were ground down to 4000 grit utilizing SiC abrasive papers and mechanically polished in a colloidal silica suspension. Specimens were finally vibro-polished using oxide polishing suspension (OPS) with a particle size of 0.04 μm for 16 h. GBs and grain sizes were analyzed based on values obtained via the TSL OIM 6 analysis software. Energy-dispersive (ED) X-ray diffraction (XRD) measurements were carried out utilizing a system equipped with a Ketek AXAS-M H80 (SDD) detector and a tungsten tube operated at 60 kV and 40 mA. The distance between the specimen and the detector was 340 mm.

3. Results and Discussion

3.1. Microstructural Evolution

A representative overview micrograph of the FSP specimen is shown in **Figure 2a**. Different regions, i.e., stir zone (SZ), heat affected zone (HAZ), thermo-mechanically affected zone (TMAZ) and BM, can be distinguished. Advancing and retreating sides as well as BD are marked on the overview image. As shown at higher magnification (**Figure 2c** and **2d**), the scanning pattern can be clearly distinguished for the as-built BM. The micrograph captured from the SZ and TMAZ (**Figure 2b**) confirms that the laser scanning pattern diminished upon FSP. In the remainder of the present work, changes in the microstructure of the as-built component upon FSP are assessed using additional characterization techniques.

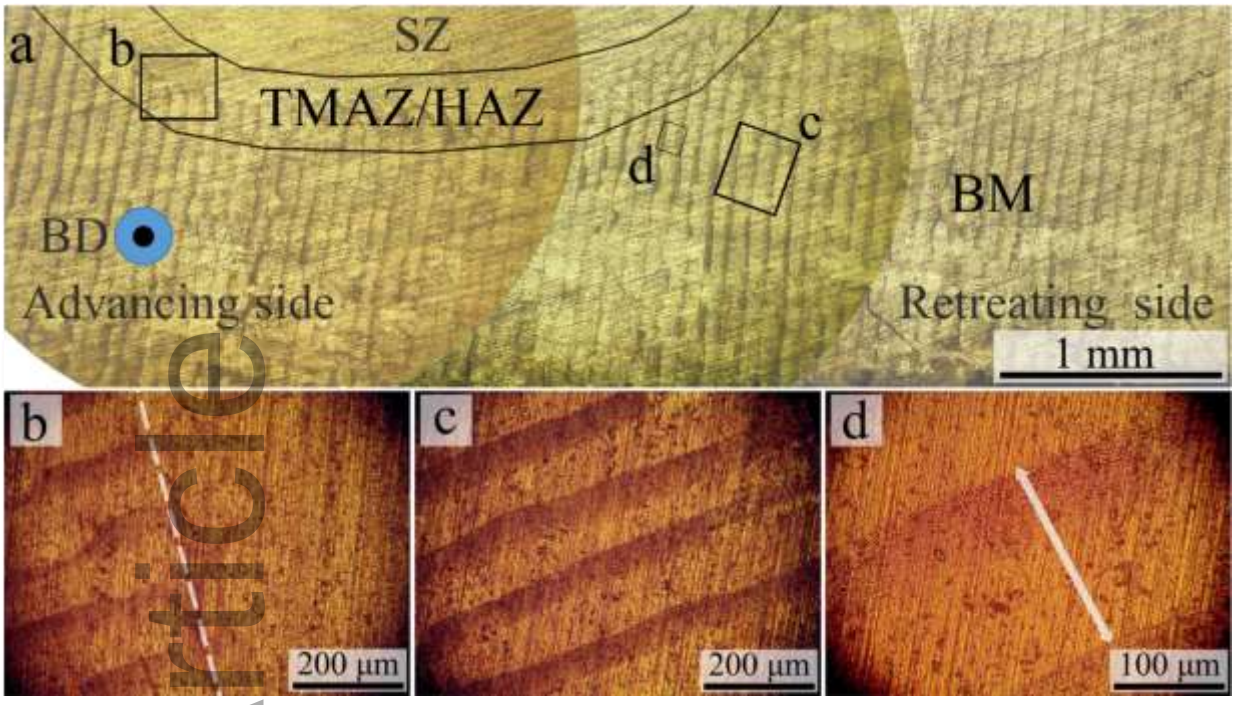

Figure 2. (a) Overview micrograph being representative for the FSP specimen captured by optical microscopy; (b-d) micrographs of the rectangular regions marked in the overview image taken at higher magnifications; (b) was captured from the TMAZ/HAZ, (c) and (d) were taken from the BM.

BSE contrast images of the as-built and FSP specimens are shown in **Figure 3**. As-built specimens consists of coarse grains being elongated in the direction of the thermal gradient and BD, respectively (**Figure 3a** and **3b**). A high density of internal defects like pores was not found in the as-built condition revealing robustness of parameters used for manufacturing of the 316L parts via PBF-LB/M. The coarse, elongated grains are the result of epitaxial grain growth commonly observed in PBF-LB/M processes when the direction of the thermal gradient remains aligned with BD during the PBF-LB/M process [4][35][36]. The BSE contrast images of the FSP specimen reveal that post-processing remarkably altered the microstructure of the 316L stainless steel. At low magnification (**Figure 3c**), the so-called onion ring pattern can be seen in case of the FSP part. The onion rings are a well-known indicator of material transport phenomena during FSP [37]. Examination of the FSP specimens at higher magnification (**Figure 3d**) reveal that due to the employment of FSP, a considerable grain refinement can be achieved for the 316L stainless steel processed via PBF-LB/M.

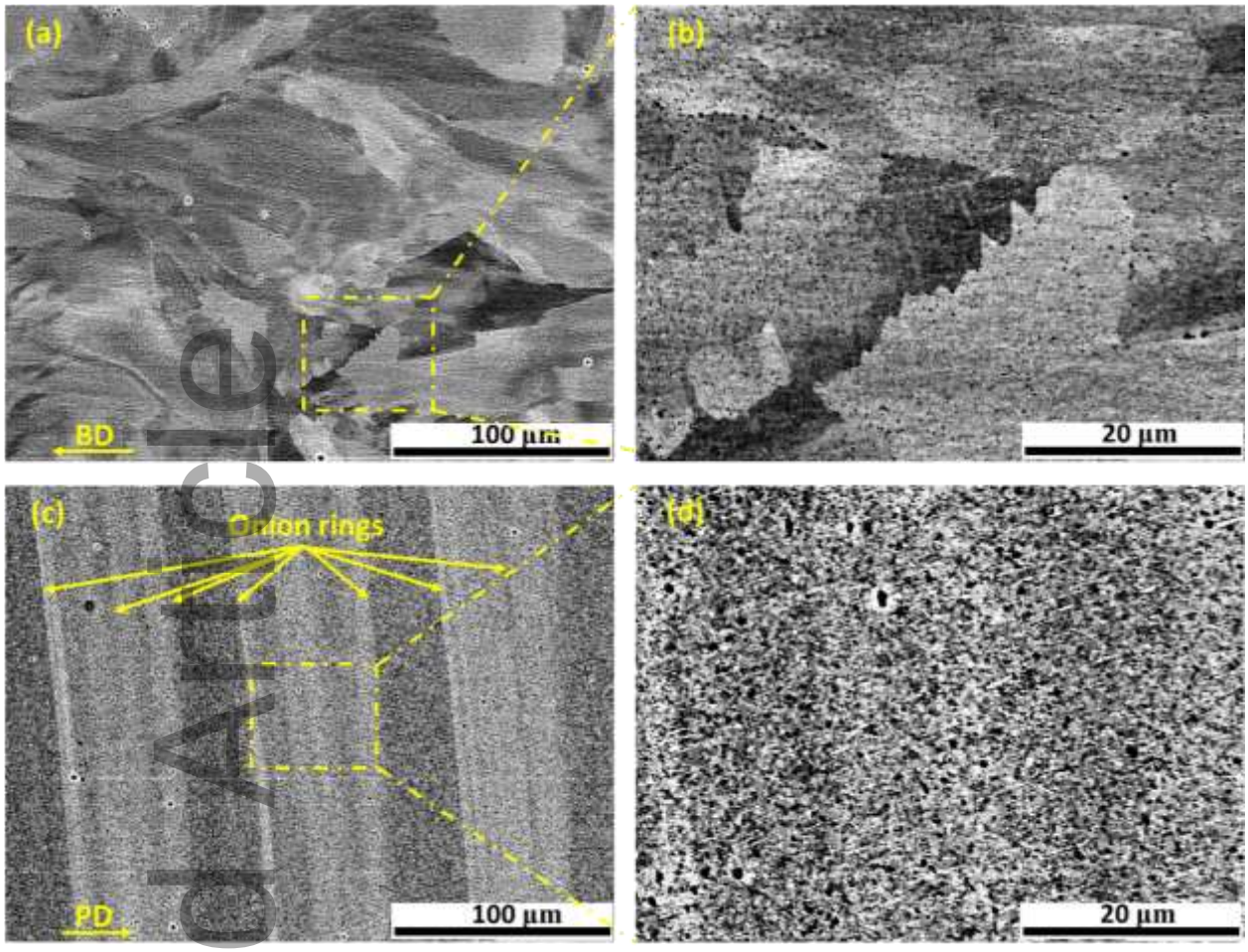

Figure 3. BSE contrast images of (a), (b) as-built and (c), (d) FSP specimens; details of respective BSE images at higher magnification are displayed and marked with yellow dashed rectangles. The BD and process direction (PD) are marked by arrows.

For in-depth analysis of microstructural evolution and a better understanding of underlying mechanisms, EBSD studies were also considered in present work as highlighted in **Figure 4**. Low-angle grain boundaries (LAGBs) and high-angle grain boundaries (HAGBs) are indicated by white and black lines, respectively. Furthermore, plots of misorientation angle versus number fraction are assessed as shown in **Figure 4e** and **4f**. In case of the as-built condition <001> oriented grains parallel to BD can be seen in the center of the probed region (**Figure 4a**). In the lower and upper sides of the captured EBSD micrograph, a few <111> oriented grains parallel to BD are evident as well. For detailed texture analysis, the (100), (110), and (111) pole figures of the as-built 316L are illustrated in **Figure 5a** revealing the formation of a strong {100} texture component (with a texture strength of about 9) alongside BD. The presence of <001> oriented grains was already numerously reported for 316L stainless steel processed via PBF-LB/M. Direction of heat flow and thermal gradient were reported to be the key elements promoting epitaxy [14][38]. Basically, the growth of grains in the orientation of <001> is favored in alloys with cubic crystals [4]. Another important

finding of the EBSD analysis, which needs to be discussed in the following, is the characteristic appearance of the grain boundaries. A relatively high fraction (0.61) of LAGBs was observed for the as-built specimen highlighting the presence of substructures in this condition (**Figure 4e**). The influence of these substructures on the mechanical properties of 316L stainless steel is well-discussed in literature [4][15]. Previous results obtained implied that these substructures impede dislocation motion and eventually result in the strengthening of the material. PBF-LB/M process parameters are responsible for the characteristics of the formed substructures [39]. Grain size distributions of both conditions are shown in **Figure 4c** and **4d**. The average grain size of the as-built specimen was determined to be 179 μm with a high standard deviation of 34 μm. Based on the analysis of the area fraction versus grain diameter of the as-built specimen, it can be deduced that the grain size distribution is very wide in this condition verifying the simultaneous presence of coarse and relatively fine grains. Such a bimodal microstructure with a wide grain size distribution can have a significant effect on the mechanical properties of the material [40]. This aspect will be further elaborated in the following chapter.

The EBSD micrograph and the characteristic grain size distribution of the FSP specimens are shown in **Figure 4b**. Upon FSP, the bimodal microstructure of the as-built 316L is transformed into an UFG microstructure with an average grain size of 1.2 μm and a corresponding standard deviation of 0.4 μm. The grain size distribution of the FSP specimen displayed in **Figure 4d** confirms that the microstructure of this condition is unimodal and consists of equiaxed grains with grain diameters less than 2 μm. EBSD characterization of GBs revealed that the fraction of HAGBs is profoundly higher in the FSP condition compared to that of the as-built counterpart attesting the formation of newly recrystallized grains (**Figure 4e** and **4f**). Therefore, grain fragmentation and the pronounced increase of the workpiece temperature during FSP are responsible for the recrystallization of the initial microstructure and transformation of the bimodal into a unimodal UFG microstructure [41]. It is also worth noting that despite a preferred <001> orientation in the as-built condition, fine equiaxed grains are characterized by randomized orientation in the FSP specimen.

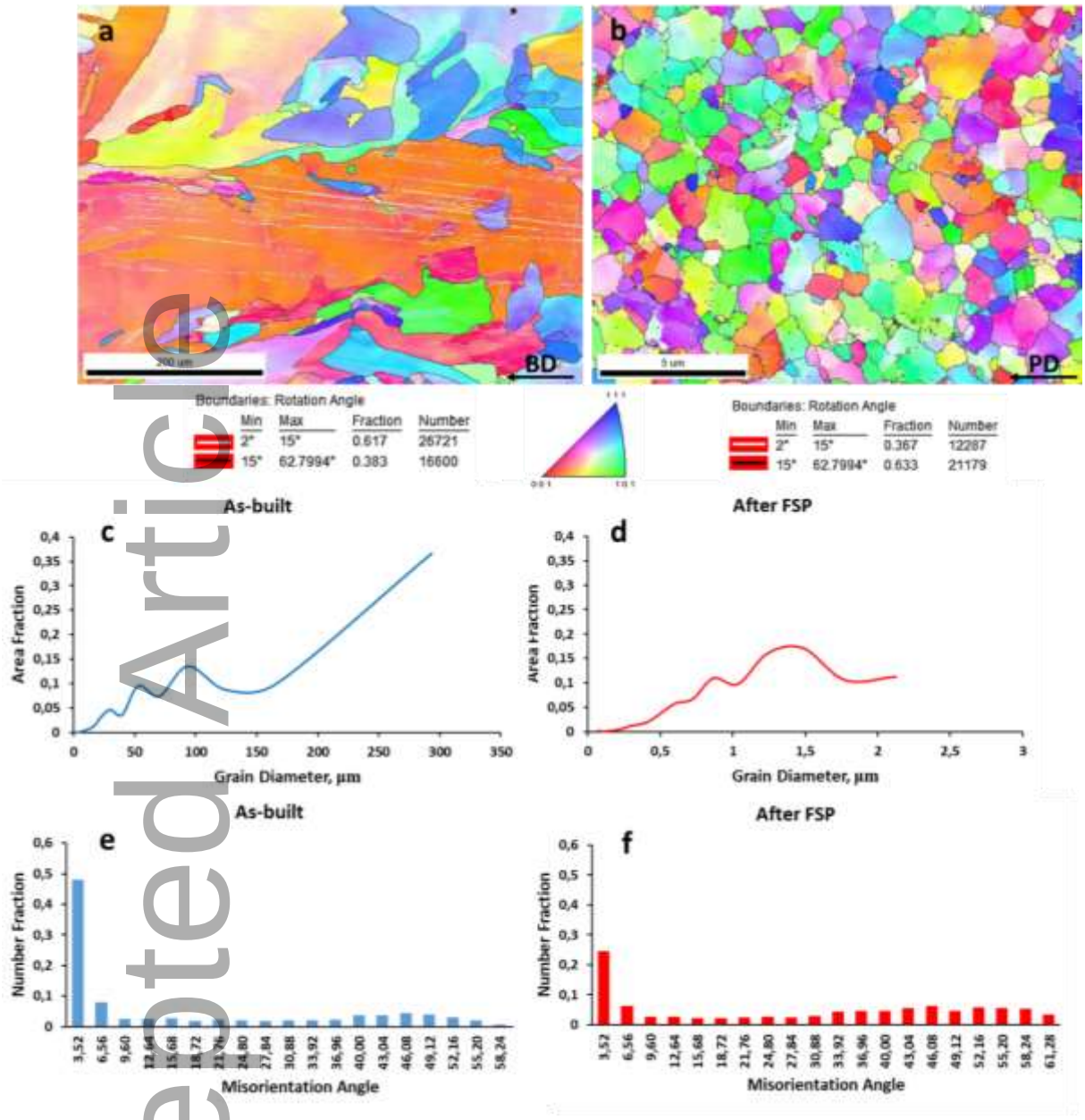

Figure 4. (a), (b) EBSD inverse pole figure (IPF) maps, (c), (d) corresponding grain size distributions and (e), (f) misorientation angles of as-built and FSP specimens along BD and PD, respectively; the standard triangle displayed in the figure refers to color coding (with respect to BD).

In **Figure 5b**, the (100), (110), and (111) pole figures of the SZ are shown confirming that FSP has significantly changed the strong texture of the BM. From **Figure 5b**, it can be deduced that characteristic shear texture components of $A_1^*(\{111\}\langle\bar{1}\bar{1}2\rangle)$, $A_2^*(\{111\}\langle11\bar{2}\rangle)$, and $C(\{001\}\langle110\rangle)$ with an intensity of 2.2 are formed in the SZ [42]. In previous studies, FSP was found to be effective for the grain refinement in 316L plates processed via conventional techniques, e.g., cold working [2][25][26][41]. It is well documented that during FSP of materials with low stacking fault energy (SFE), continuous and discontinuous dynamic recrystallization (CDRX and DDRX) are the governing

mechanisms of grain structure formation [43]. In present work, DDRX seems to be the dominant factor due to the finally weak texture intensity, which is known to be the result of nucleation and growth stages. EBSD analysis and BSE studies clearly lay out that the FSP used in the present study considerably affects the grain size, texture and homogeneity of microstructure. However, changes in the evolution of microstructure have to be linked to the variations in the mechanical properties for direct GB engineering and development of additively manufactured 316L components being characterized by superior performance. Thus, the following chapter mainly focuses on the mechanical behavior of as-built and FSP 316L specimens.

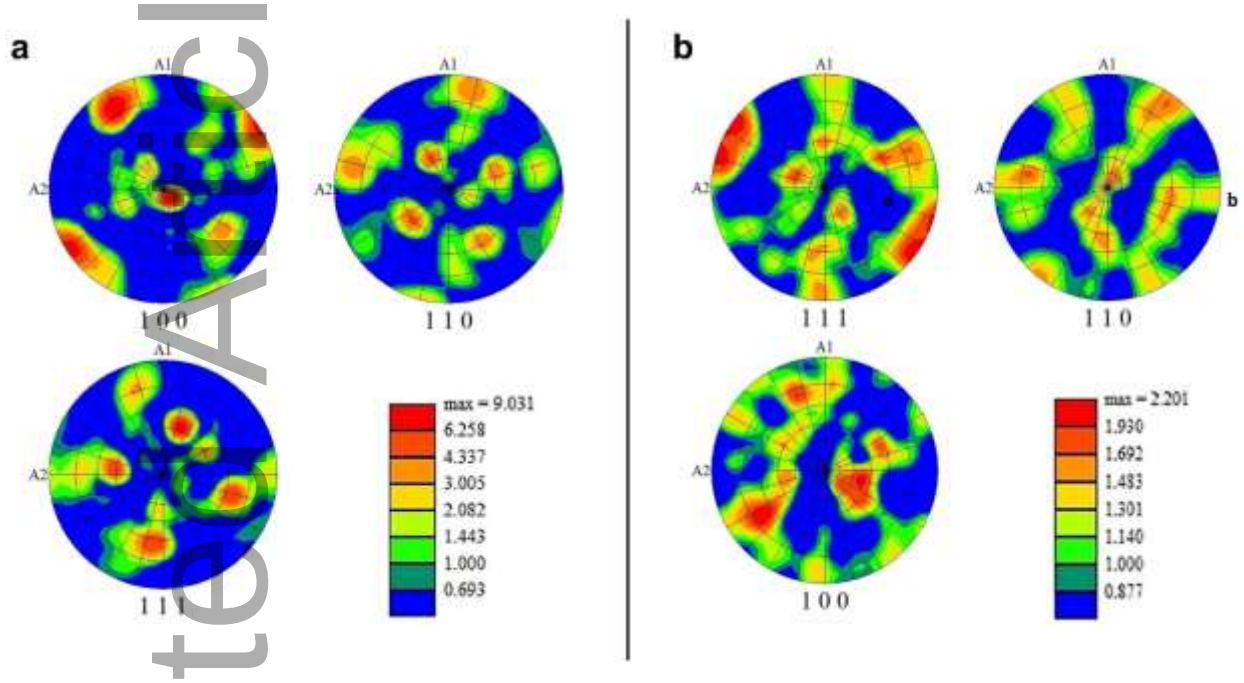

Figure 5. (100), (110), and (111) pole figures of (a) as-built 316L and (b) FSP 316L in conjunction with (111) ideal simple shear texture components in face centered cubic (FCC) materials. A1 and A2 are the normal directions to the BD. Texture analysis was conducted by the assessment of EBSD data.

3.2. Mechanical Response

Mechanical properties of both as-built and FSP conditions were characterized using microhardness measurements and tensile tests. The average microhardness of 316L stainless steel processed via PBF-LB/M was measured to be 213.4 ± 6.5 HV 0.5. It was previously reported that depending on the powder characteristics, the parameters set used in the AM process and resulting microstructure, the hardness value of as-built 316L is typically in the range of 200 to 291 HV [20][22][39][44]–[48]. Microhardness measurement on the FSP specimen showed that this process is able to increase the hardness of this alloy up to 310.2 ± 2.6 HV. Higher standard deviation in terms of the microhardness value of the as-built specimen in comparison to the FSP counterpart can be attributed to the presence of a bimodal microstructure in the former.

Stress-strain curves of the as-built and the FSP 316L specimens are displayed in **Figure 6**. Although only one representative curve for each condition is shown, three tensile experiments were carried out to check the repeatability. The repeatability of the tensile experiments was very good. The values of EF, YS and UTS for the as-built condition were found to be 65 %, 311 MPa and 511 MPa, respectively. Tensile test results implied that upon processing of 316L via PBF-LB/M, a ductile component with superior mechanical properties compared to that of conventionally manufactured components can be achieved [49]. It is also worth noting that the as-built material is characterized by steady strain hardening [8][9][50]. High ductility of the as-built specimen obtained in the tensile experiments may be attributed to the occurrence of slip and twinning-induced plasticity (TWIP) effect [51][52], however, this is not further assessed in present work.

By comparing the stress-strain curves of both conditions, it can be deduced that FSP could highly enhance the strength of the 316L stainless steel, however, with a gradual loss in ductility. EF, YS and UTS of FSP specimens were measured to be 24%, 549 MPa and 826 MPa, respectively. Values obtained in microhardness measurements and tensile tests revealed that upon FSP, microhardness, YS and UTS of this material can be increased by 45%, 77% and 62%, respectively, while EF was degraded by 63%. FSP processing of AM 316L stainless steel was already found to be capable of enhancing strength before, however, only an improvement of 18% in UTS was reported [33]. YS, UTS and EF values obtained in the previously published research work are compared with the results of the present study (**Figure 6b**). The significant grain refinement revealed by the results of microstructural investigations discussed above is the main reason for such a substantial enhancement in mechanical properties upon FSP. Basically, strengthening of different steels via grain refinement was the topic of many research works [2][33][53]–[55] since this mechanism was found to be very effective for metallic materials in general. For in-depth analysis and assessment of the obtained results, the relationship between mechanical properties and underlying elementary mechanisms are discussed in the remainder of present work.

a

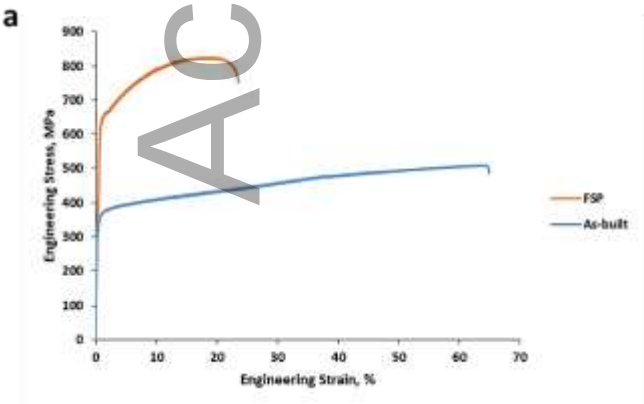

b

Condition	YS (MPa)	UTS (MPa)	ε_f (%)
As-built-present study	311	511	65
FSP-present study	549	826	24
As-built-Peng et al. [33]	522	724	37
FSP-Peng et al. [33]	674	856	37

Figure 6. (a) Stress-strain curves of the as-built and the FSP 316L specimens; (b) Tabular representation of the YS, UTS and ε_f obtained in the present study and the study by Peng et al. [33].

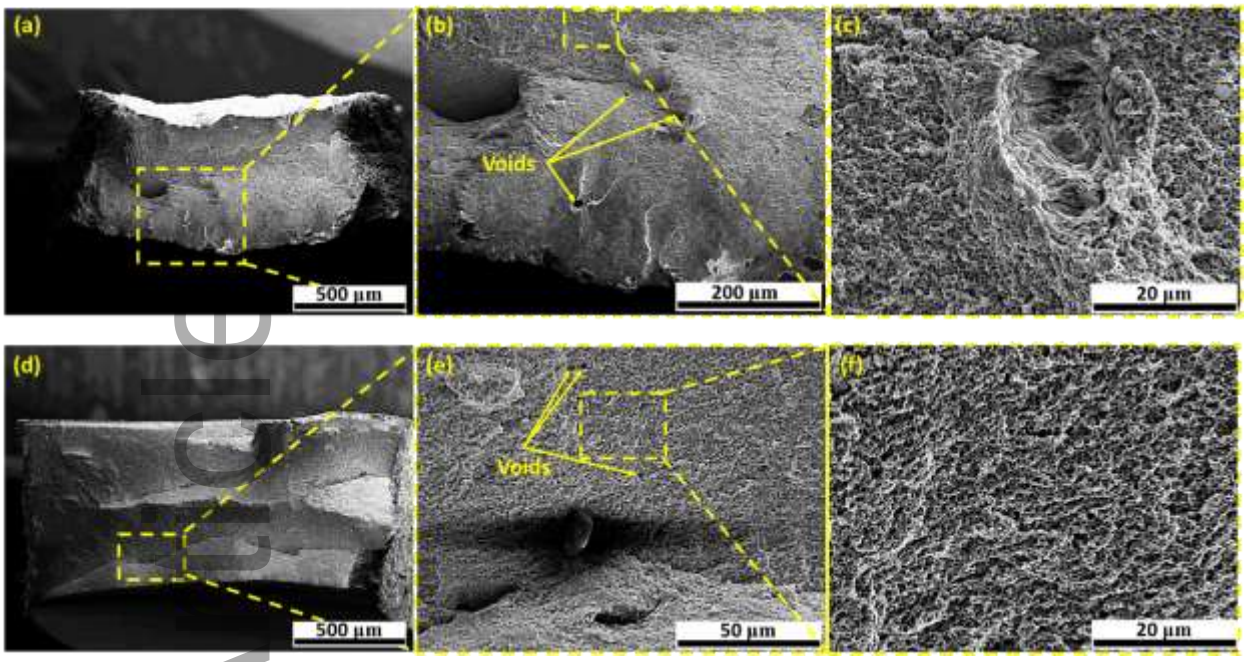

Figure 7. SEM fracture surfaces upon tensile testing of (a-c) the as-built and (d-f) the FSP 316L specimens. Details of respective fracture surfaces at higher magnification are displayed and marked with yellow dashed rectangles. Voids captured on the fracture surfaces are marked by yellow arrows.

Characteristic fracture surfaces upon tensile testing of the as-built and the FSP 316L specimens are shown in **Figure 7**. Dimples on the fracture surfaces of both as-built and FSP samples confirm ductile failure. This observation is also corroborated with the mechanical response of both specimens exceeding elongation levels of above 20 %. Microvoids can be observed on the fracture surfaces of both conditions, however, the voids captured on the SEM images of the as-built specimen are slightly larger in size. This can be related to the transformation of coarse voids into fine voids during SPD [28].

3.3. Process-microstructure-property relationships

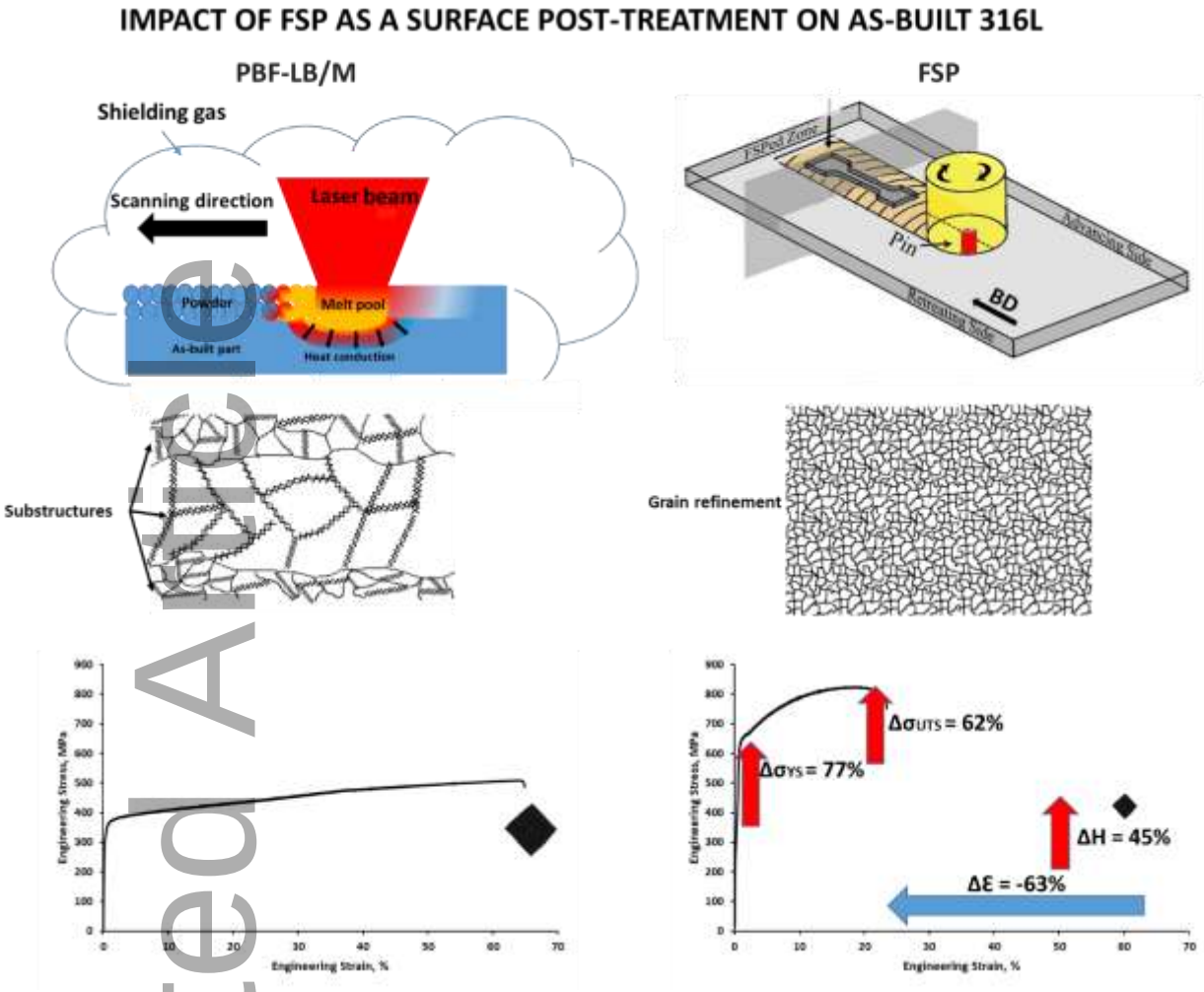

Figure 8. Schematics highlighting the influence of FSP on the as-built microstructure and mechanical properties of 316L stainless steel. Processes employed, differences in microstructure and the mechanical properties are shown in the upper, middle and lower rows, respectively.

Figure 8 schematically depicts most relevant process-microstructure-property relationships deduced from the results obtained. PBF-LB/M processing promotes the formation of a bimodal microstructure containing a high-density of substructures. As it is well-known, the surface of the previously solidified layer assists the heterogeneous solidification and reduces surface energy due to the bonding across the subsurface [56]–[58]. This assists the formation of columnar grains with orientations parallel to the orientation of the previously formed layer. Microstructural assessment in the present study revealed that substructures and LAGBs, respectively, were formed in the as-built 316L stainless steel. Formation of substructures in 316L can be rationalized based on the high solidification rate in PBF-LB/M. High solidification rates promote in increase in the concentration of vacancies and eventually increase in dislocation density due to the aggregation of introduced

vacancies [59][60]. Besides, melting of subsequent layers generates high temperatures facilitating the heat treatment of the already solidified substrate containing a high density of dislocations [56][61]–[63].

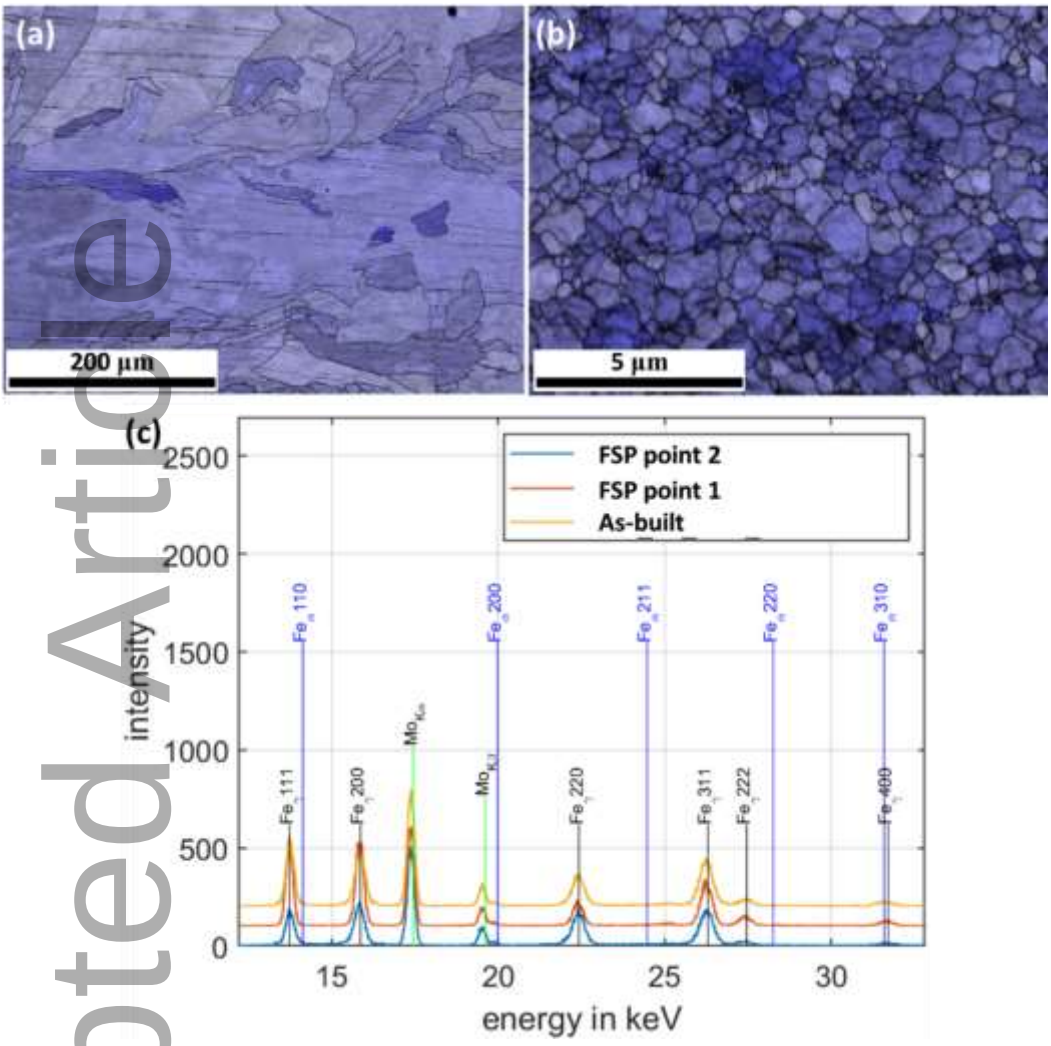

Figure 9. Grain average misorientation (GAM) maps of the (a) as-built, and (b) FSP samples, where darker colors refer to higher density of dislocations; (c) energy-dispersive X-ray diffraction patterns of as built and FSP samples. Two different regions were examined for the FSP sample.

In order to qualitatively assess the dislocation density in the as-built and the FSP specimen, grain average misorientation (GAM) maps can be employed [64]. Such GAM maps are illustrated in **Figure 9a** and **9b**, in which the darker colors refer to higher density of dislocations. Basically, the as-built 316L (**Figure 9a**) contained a considerable number of dislocations stemming from rapid solidification and intrinsic heat treatment in PBF-LB/M. It should be noted that, after FSP, the number of dislocations has been even increased (**Figure 9b**). Obviously, rearrangement of dislocations during these treatments can lead to the formation of substructures in the solidified layers. Mechanical properties of 316L fabricated via PBF-LB/M can be rationalized based on the prevailing microstructure. It is well-known that ductility of austenitic stainless steels can be

enhanced by a combination of slip and TWIP mechanisms [51][52]. The high strain hardening and UTS to YS ratio obtained for the as-built specimen may also be ascribed to the interactions between present substructures, deformation twins and dislocations generated during tensile deformation [65][66]. However, any traces related to twinning have not been found in present work, high-resolution microscopy will have to be conducted at this point, this being out of the scope of present work.

As elaborated in section 3.1, upon FSP the bimodal microstructure of the AM component with its characteristic texture was transformed into a UFG microstructure with randomized orientations. Thus, FSP diminishes potential mechanical anisotropy caused by AM. Fragmentation of initial grains and recrystallization of microstructure during SPD are responsible for grain refinement [26][28][33][67]. It is apparent that the level of grain refinement induced during SPD significantly altered the mechanical properties of the 316L stainless steel fabricated via PBF-LB/M. According to the Hall-Petch relation, grain refinement enhances the strength of metallic materials by increasing the fraction of grain boundaries impeding dislocation motion [68]–[72]. Thus, the increased hardness, YS and UTS values of the FSP specimen compared to that of the as-built counterpart are imputed to the uniformly refined microstructure. It should also be noted that the ductility of the FSP specimens is lower than that of the as-built parts. However, the FSP specimens still exhibited a fairly good ductile behavior as their ductility was found to be above 24%. Reduction in ductility of FSP specimens is due to the fact that the UFG microstructure with a high density of defects (e.g., high density of dislocations (**Figure 9**) can hardly tolerate the accumulation of dislocations. Hence, further deformation of the material promotes crack initiation in the vicinity of microstructural defects [73]–[75]. **Figure 9c** shows the results obtained by ED-XRD of as-built and FSP specimens. From this figure, it can be deduced that 316L stainless steel remains in a single FCC phase upon FSP. Although HPT as one of the SPD methods resulted in the phase transformation of additively manufactured Fe-Cr-Ni stainless steel [76], in the present study FSP as another SPD method did not lead to phase transformation in the 316L stainless steel. The higher level of SPD strain in HPT compared to that of FSP may lead to the phase transformation in stainless steels [76]. However, having a single phase could be advantageous due to moderate ductility achieved after FSP [77].

Mechanical properties achieved in the present study can be directly compared to previous work on FSP of as-built 316L available in literature [33]. Peng et al. [33] could improve hardness, YS and UTS of additively manufactured 316L stainless steel by 25%, 29% and 18%, respectively, while the present study shows that the improvement in the strength and hardness of this alloy can even reach higher levels. Herein, hardness, YS and UTS of the as-built counterpart were significantly enhanced by 45%, 77% and 62%, respectively. The more efficient improvement in comparison to literature [33] can be attributed to the coarser initial microstructure of the as-built counterpart in the present

study (179 μm (grain size obtained using the TSL OIM 6 analysis software) in comparison to 6.6 μm in [33] (grain size obtained using HKL CHANNEL5 software)) . Upon FSP, a significantly higher level of grain refinement was achieved herein as compared to that reported previously [33]. Consequently, the differences between hardness, YS and UTS values of the as-built and the FSP specimens is higher in present work. A few studies already focused on FSP and FSW of additively manufactured aluminum alloys [29]–[31]. It was found that an increase in temperature during FSP and FSW, respectively, causes the agglomeration and coarsening of Si-rich particles deteriorating the strength of the material. Fine Si networks formed in the rapid solidification process play a key role in the strengthening of additively manufactured aluminum alloys. Thus, dissolution of these networks adversely affects the mechanical properties of components. Another SPD method employed for the improvement in the strength of additively manufactured components was ECAP [28]. ECAP could even improve the YS and UTS of additively manufactured AlSi12 by 56% and 11%, respectively. By comparing the results obtained in the present study and the relevant literature, it can be deduced that SPD processing parameters (e.g., temperature and route in ECAP/HPT or travel and rotational speeds in FSP/FSW) have a significant impact on the resulting behavior and, hence, they should be adjusted accordingly for the optimization of as-built microstructures facilitating enhanced mechanical response in AM metals.

4. Conclusions

In the present study, the impact of friction stir processing on the mechanical behavior and microstructure of 316L processed via laser-based powder bed fusion of metals was explored. The following conclusions are drawn:

i. The analysis of microstructure revealed that upon friction stir processing the bimodal microstructure of the as-built condition was transformed into a unimodal ultra-fine grained microstructure. Average grain sizes of the as-built and the friction stir processed specimens were found to be 179 μm and 1.2 μm, respectively.

ii. Characterization of mechanical properties via microhardness measurements and tensile experiments showed that despite a loss in ductility, friction stir processing can enhance hardness, yield point and ultimate tensile strength of 316L processed by laser-based powder bed fusion up to 45%, 77% and 62%, respectively, due to grain refinement.

iii. Fracture analysis revealed that both friction stir processed and as-built conditions exhibited ductile failure. Finer voids captured on the fracture surfaces of the friction stir processed specimens compared to those of as-built specimens indicate that this process can be employed for densification of additively manufactured components through the transformation of coarse voids to fine voids.

iv. The anisotropic as-built microstructure, i.e., the strong texture, is replaced with equiaxed grains being characterized by random orientations. The elementary mechanism being responsible

(dynamic recrystallization), thus, effectively diminishes potential mechanical anisotropy induced during additive manufacturing.

v. Grain average misorientation maps revealed that due to rapid solidification and intrinsic heat treatment the as-built 316L is characterized by the presence of a considerable number of dislocations and specific dislocation arrangements, i.e., subgrains. Friction stir processing even resulted in further increase in dislocation density and the evolution of high-angle grain boundaries in this alloy. Energy-dispersive X-ray diffraction patterns revealed that there is no phase transformation in this alloy upon friction stir processing.

CRediT authorship contribution statement

S.V. Sajadifar: Conceptualization, Methodology, Data curation, Investigation, Writing-original draft, Writing-review & editing. **A. Hosseinzadeh**: Conceptualization, Methodology, Data curation, Investigation, Writing-review & editing. **J. Richter**: Methodology, Data curation, Investigation, Writing-original draft, Writing-review & editing. **M. Krochmal**: Data curation, Investigation. **T. Wegener**: Methodology, Data curation, Investigation, Writing-original draft, Writing-review & editing. **A. Bolender:** Data curation, Investigation. **A. Heidarzadeh**: Methodology, Investigation, Writing-original draft, Writing-review & editing, Supervision. **T. Niendorf**: Resources, Project administration, Writing-review & editing, Supervision. **G.G. Yapici**: Resources, Project administration, Writing-review & editing, Supervision.

Declaration of competing interest

The authors declare that they have no known competing financial interests or personal relationships that could have appeared to influence the work reported in this paper.

Acknowledgements

This investigation is supported by the BAGEP Award of the Science Academy, Turkey. The system used for additive manufacturing is provided through the funding by DFG under project no. 346979276.

References

[1] R. Casati, J. Lemke, M. Vedani, *J. Mater. Sci. Technol.* **2016**, *32*, 738.

[2] S.S. Rezaei-Nejad, A. Abdollah-zadeh, M. Hajian, F. Kargar, R. Seraj, *Procedia Mater. Sci.* **2015**, *11*, 397.

[3] G.G. Yapici, I. Karaman, Z.P. Luo, H.J. Maier, Y.I. Chumlyakov, *J. Mater. Res.* **2004**, *19*, 2268.

[4] F. Brenne, T. Niendorf, *Mater. Sci. Eng. A* **2019**, *764*, 138186.

[5] P.S. Kumar, S.G. Acharyya, *Mater. Today Proc.* **2019**, *15*, 138.

[6] A. Weisenburger, C. Schroer, A. Jianu, A. Heinzel, J. Konys, H. Steiner, G. Müller, C. Fazio, A. Gessi, S. Babayan, A. Kobzova, L. Martinelli, K. Ginestar, F. Balbaud-Célerier, F.J. Martín-Muñoz, L. Soler Crespo, *J. Nucl. Mater.* **2011**, *415*, 260.

[7] V.A. Andrei, C. Radulescu, V. Malinovschi, A. Marin, E. Coaca, M. Mihalache, C.N. Mihailescu, I.D. Dulama, S. Teodorescu, I.A. Bucurica, *Coatings 2020, Vol. 10, Page 318* **2020**, *10*, 318.

[8] G.Z. Liu, N.R. Tao, K. Lu, *J. Mater. Sci. Technol.* **2010**, *26*, 289.

[9] T. Nakanishi, T. Tsuchiyama, H. Mitsuyasu, Y. Iwamoto, S. Takaki, *Mater. Sci. Eng. A* **2007**, *460–461*, 186.

[10] P.S. Korinko, S.H. Malene, *Pract. Fail. Anal. 2001 14* **2001**, *1*, 61.

[11] J. Xin, H. Zhang, W. Sun, C. Huang, S. Wang, J. Wei, W. Wang, Z. Fang, D. Wu, L. Li, *Cryogenics (Guildf).* **2021**, *118*, 103344.

[12] A. Röttger, K. Geenen, M. Windmann, F. Binner, W. Theisen, *Mater. Sci. Eng. A* **2016**, *678*, 365.

[13] T. Niendorf, S. Leuders, A. Riemer, F. Brenne, T. Tröster, H.A. Richard, D. Schwarze, *Adv. Eng. Mater.* **2014**, *16*, 857.

[14] T. Niendorf, S. Leuders, A. Riemer, H.A. Richard, T. Tröster, D. Schwarze, *Metall. Mater. Trans. B* **2013**, *44*, 794.

[15] A. Riemer, S. Leuders, M. Thöne, H.A. Richard, T. Tröster, T. Niendorf, *Eng. Fract. Mech.* **2014**, *120*, 15.

[16] M. Yakout, M.A. Elbestawi, S.C. Veldhuis, *Int. J. Adv. Manuf. Technol. 2017 955* **2017**, *95*, 1953.

[17] M. Schmidt, M. Merklein, D. Bourell, D. Dimitrov, T. Hausotte, K. Wegener, L. Overmeyer, F. Vollertsen, G.N. Levy, *CIRP Ann.* **2017**, *66*, 561.

[18] D. Herzog, V. Seyda, E. Wycisk, C. Emmelmann, *Acta Mater.* **2016**, *117*, 371.

[19] L.E. Murr, S.M. Gaytan, D.A. Ramirez, E. Martinez, J. Hernandez, K.N. Amato, P.W. Shindo, F.R. Medina, R.B. Wicker, *J. Mater. Sci. Technol.* **2012**, *28*, 1.

[20] W. Chen, G. Yin, Z. Feng, X. Liao, *Met. 2018, Vol. 8, Page 729* **2018**, *8*, 729.

[21] E. Liverani, S. Toschi, L. Ceschini, A. Fortunato, *J. Mater. Process. Technol.* **2017**, *249*, 255.

[22] S. Gao, Z. Hu, M. Duchamp, P.S.S.R. Krishnan, S. Tekumalla, X. Song, M. Seita, *Acta Mater.* **2020**, *200*, 366.

[23] F. Abdi, A. Eftekharian, D. Huang, R.B. Rebak, M. Rahmane, V. Sundararaghavan, A. Kanyuck, S.K. Gupta, S. Arul, V. Jain, Y. Hu, K. Nikbin, *Forces Mech.* **2021**, *4*, 100033.

[24] I.A. Segura, L.E. Murr, C.A. Terrazas, D. Bermudez, J. Mireles, V.S.V. Injeti, K. Li, B. Yu,

R.D.K. Misra, R.B. Wicker, *J. Mater. Sci. Technol.* **2019**, *35*, 351.

[25] Y.C. Chen, H. Fujii, T. Tsumura, Y. Kitagawa, K. Nakata, K. Ikeuchi, K. Matsubayashi, Y. Michishita, Y. Fujiya, J. Katoh, *Sci. Technol. Weld. Join.* **2013**, *14*, 197.

[26] M. Hajian, A. Abdollah-zadeh, S.S. Rezaei-Nejad, H. Assadi, S.M.M. Hadavi, K. Chung, M. Shokouhimehr, *Mater. Des.* **2015**, *67*, 82.

[27] M. Hajian, A. Abdollah-Zadeh, S.S. Rezaei-Nejad, H. Assadi, S.M.M. Hadavi, K. Chung, M. Shokouhimehr, *Appl. Surf. Sci.* **2014**, *308*, 184.

[28] A. Hosseinzadeh, A. Radi, J. Richter, T. Wegener, S.V. Sajadifar, T. Niendorf, G.G. Yapici, *J. Manuf. Process.* **2021**, *68*, 788.

[29] G. Moeini, S.V. Sajadifar, T. Wegener, C. Rössler, A. Gerber, S. Böhm, T. Niendorf, *J. Mater. Res. Technol.* **2021**, *12*, 1446.

[30] G. Moeini, S.V. Sajadifar, T. Engler, B. Heider, T. Niendorf, M. Oechsner, S. Böhm, *Metals (Basel).* **2020**, *10*, 85.

[31] G. Moeini, S. V. Sajadifar, T. Wegener, F. Brenne, T. Niendorf, S. Böhm, *Mater. Sci. Eng. A* **2019**, *764*, 138189.

[32] S.M. Yusuf, M. Hoegden, N. Gao, *Int. J. Adv. Manuf. Technol.* **2020**, *106*, 4321.

[33] P. Peng, K. Wang, W. Wang, P. Han, T. Zhang, Q. Liu, S. Zhang, H. Wang, K. Qiao, J. Liu, *Mater. Charact.* **2020**, *163*, 110283.

[34] S.M. Yusuf, Y. Chen, N. Gao, *Met. 2021, Vol. 11, Page 1553* **2021**, *11*, 1553.

[35] H. Helmer, A. Bauereiß, R.F. Singer, C. Körner, *Mater. Sci. Eng. A* **2016**, *668*, 180.

[36] J. Richter, S. V. Sajadifar, T. Niendorf, *Addit. Manuf.* **2021**, *47*, 102346.

[37] G.R. Cui, Z.Y. Ma, S.X. Li, *Scr. Mater.* **2008**, *58*, 1082.

[38] S.A. David, J.M. Vitek, *Int. Mater. Rev.* **2013**, *34*, 213.

[39] T. Kurzynowski, K. Gruber, W. Stopyra, B. Kuźnicka, E. Chlebus, *Mater. Sci. Eng. A* **2018**, *718*, 64.

[40] B. Flipon, C. Keller, L.G. de la Cruz, E. Hug, F. Barbe, *Mater. Sci. Eng. A* **2018**, *729*, 249.

[41] H.S. Arora, A. Ayyagari, J. Saini, K. Selvam, S. Riyadh, M. Pole, H.S. Grewal, S. Mukherjee, *Sci. Reports 2019 91* **2019**, *9*, 1.

[42] L.S. Tóth, K.W. Neale, J.J. Jonas, *Acta Metall.* **1989**, *37*, 2197.

[43] A. Heidarzadeh, S. Mironov, R. Kaibyshev, G. Çam, A. Simar, A. Gerlich, F. Khodabakhshi, A. Mostafaei, D.P. Field, J.D. Robson, A. Deschamps, P.J. Withers, *Prog. Mater. Sci.* **2021**, *117*, 100752.

[44] J. Luo, X. Jia, R. Gu, P. Zhou, Y. Huang, J. Sun, M. Yan, *Met. 2018, Vol. 8, Page 548* **2018**, *8*, 548.

[45] Z. Sun, X. Tan, S.B. Tor, W.Y. Yeong, *Mater. Des.* **2016**, *104*, 197.

[46] S. Yusuf, Y. Chen, R. Boardman, S. Yang, N. Gao, *Metals (Basel).* **2017**, *7*, 64.

[47] J.A. Cherry, H.M. Davies, S. Mehmood, N.P. Lavery, S.G.R. Brown, J. Sienz, *Int. J. Adv. Manuf. Technol. 2014 765* **2014**, *76*, 869.

[48] D. Wang, C. Song, Y. Yang, Y. Bai, *Mater. Des.* **2016**, *100*, 291.

[49] I. Tolosa, F. Garciandía, F. Zubiri, F. Zapirain, A. Esnaola, *Int. J. Adv. Manuf. Technol. 2010 515* **2010**, *51*, 639.

[50] W. Zieliński, A.A. Abduluyahed, K.J. Kurzydłowski, *Mater. Sci. Eng. A* **1998**, *249*, 91.

[51] M. Calmunger, G. Chai, R. Eriksson, S. Johansson, J.J. Moverare, *Metall. Mater. Trans. A Phys. Metall. Mater. Sci.* **2017**, *48*, 4525.

[52] Z. Sun, X. Tan, S.B. Tor, C.K. Chua, *NPG Asia Mater. 2018 104* **2018**, *10*, 127.

[53] T. Niendorf, H.J. Maier, D. Canadinc, I. Karaman, *Mater. Sci. Eng. A* **2009**, *503*, 160.

[54] I. Karaman, G.G. Yapici, Y.I. Chumlyakov, I. V. Kireeva, *Mater. Sci. Eng. A* **2005**, *410–411*, 243.

[55] N. Merah, M.A. Azeem, H.M. Abubaker, F. Al-Badour, J. Albinmousa, A.A. Sorour, *Mater. 2021, Vol. 14, Page 5023* **2021**, *14*, 5023.

[56] A. Röttger, J. Boes, W. Theisen, M. Thiele, C. Esen, A. Edelmann, R. Hellmann, *Int. J. Adv. Manuf. Technol.* **2020**, *108*, 769.

[57] F. Hengsbach, P. Koppa, M.J. Holzweissig, M.E. Aydinöz, A. Taube, K.P. Hoyer, O. Starykov, B. Tonn, T. Niendorf, T. Tröster, M. Schaper, *Prog. Addit. Manuf.* **2018**, *3*, 221.

[58] R. Elliott, *Cast Iron Technol.* **1988**, 91.

[59] T. Haraguchi, K. Yoshimi, M.H. Yoo, H. Kato, S. Hanada, A. Inoue, *Acta Mater.* **2005**, *53*, 3751.

[60] W. Ammon, *Springer Handbooks* **2006**, 101.

[61] J. Boes, A. Röttger, C. Mutke, C. Escher, W. Theisen, *Addit. Manuf.* **2018**, *23*, 170.

[62] J. Ning, D.E. Sievers, H. Garmestani, S.Y. Liang, *Int. J. Precis. Eng. Manuf. - Green Technol.* **2020**, *7*, 585.

[63] C.J.J. Torrent, S. Wackenrohr, J. Richter, C.E. Sobrero, S. Degener, P. Krooß, H.J. Maier, T. Niendorf, *Adv. Eng. Mater.* **2021**, *23*, 2100018.

[64] A. Heidarzadeh, A. Chabok, R. Taherzadeh Mousavian, Y. Pei, *Philos. Mag.* **2019**, *100*, 337.

[65] M. Ziętala, T. Durejko, R. Panowicz, M. Konarzewski, *Mater. 2020, Vol. 13, Page 4893* **2020**, *13*, 4893.

[66] D. Kuhlmann-Wilsdorf, N.R. Comins, *Mater. Sci. Eng.* **1983**, *60*, 7.

[67] W. Tang, X. Yang, S. Li, H. Li, *J. Mater. Process. Technol.* **2019**, *271*, 189.

[68] A. Hosseinzadeh, S. Salahi, A. Radi, S.V. Sajadifar, G.G. Yapici, *J. Mater. Eng. Perform.* **2021**, *30*, 8643.

[69] S.V. Sajadifar, C. Atli, G.G. Yapici, *Mater. Lett.* **2019**, *244*, 100.

[70] B.P. Kashyap, K. Tangri, *Acta Metall. Mater.* **1995**, *43*, 3971.

[71] K.K. Singh, S. Sangal, G.S. Murty, *Mater. Sci. Technol.* **2013**, *18*, 165.

[72] X. Feaugas, H. Haddou, *Metall. Mater. Trans. A 2003 3410* **2003**, *34*, 2329.

[73] D. Jia, Y.M. Wang, K.T. Ramesh, E. Ma, Y.T. Zhu, R.Z. Valiev, *Appl. Phys. Lett.* **2001**, *79*, 611.

[74] Y.T. Zhu, X. Liao, *Nat. Mater. 2004 36* **2004**, *3*, 351.

[75] Z. Budrovic, H. Van Swygenhoven, P.M. Derlet, S. Van Petegem, B. Schmitt, *Science.* **2004**, *304*, 273.

[76] A. Heidarzadeh, M. Neikter, N. Enikeev, L. Cui, F. Forouzan, R.T. Mousavian, *Mater. Sci. Eng. A* **2021**, *811*, 141086.

[77] G.G. Yapici, *Mater. Letters* **2020**, *279*, 128443.

Table of Contents Statement and Graphical Abstract

This work highlights the utilization of friction stir processing as a novel technique for the surface modification of additive manufactured 316L stainless steel. Mechanical behavior and microstructural evolution were exploited to establish the process-microstructure-property relationships in the severely deformed alloy. Provision of an ultra-fine grained microstructure demonstrates the potential of severe plastic deformation as a post-processing tool for densification and thereby leading to the improvement of the mechanical properties in additively manufactured parts.

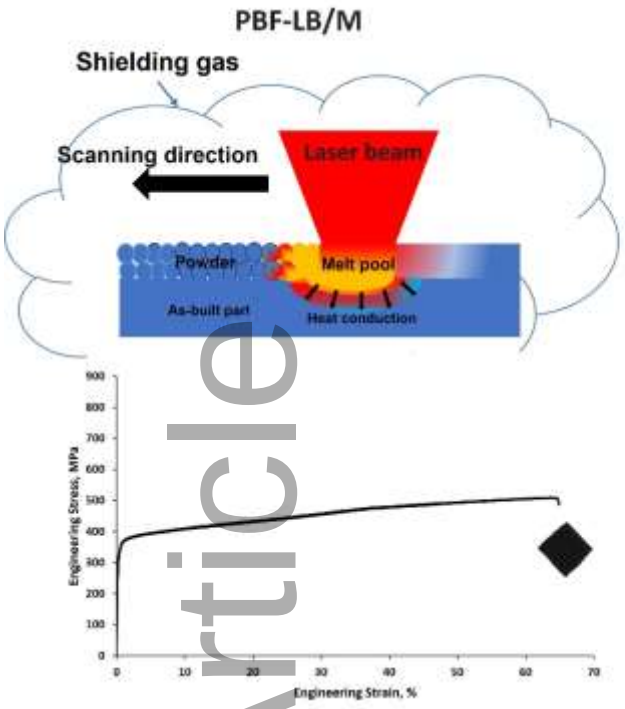

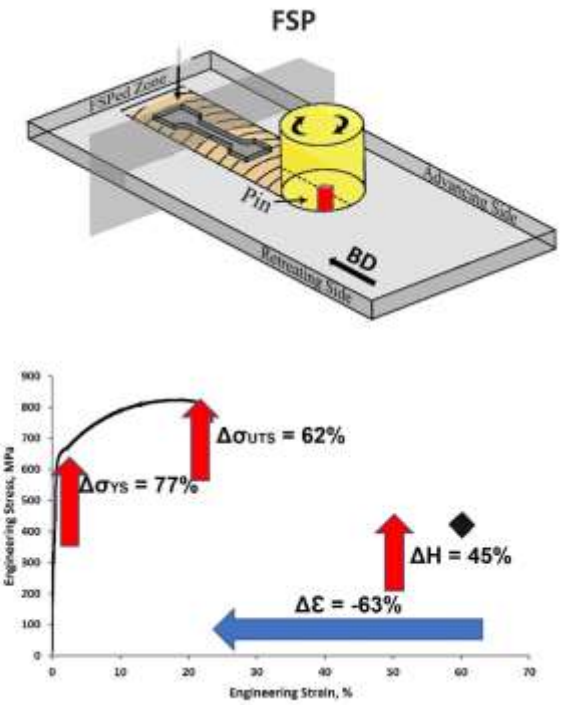

Autorenversion von: Sajadifar, S.V., Hosseinzadeh, A., Richter, J., Krochmal, M., Wegener, T., Bolender, A., Heidarzadeh, A., Niendorf, T. and Yapici, G.G. (2022), On the Friction Stir Processing of Additive-Manufactured 316L Stainless Steel. Adv. Eng. Mater., 24: 2200384. https://doi.org/10.1002/adem.202200384